













Ferroelectric to paraelectric structural transition in LiTaO₃ and LiNbO₃

Felix Bernhardt ^{1,2,*}, Leonard M. Verhoff ¹, Nils A. Schäfer ¹, Alexander Kapp ¹, Christa Fink ^{1,2}, Wafaa Al Nachwati ¹, Umar Bashir,³ Detlef Klimm ³, Fatima El Azzouzi,⁴ Uliana Yakhnevych ⁴, Yuriy Suhak,⁴ Harald Schmidt ⁵, Klaus-Dieter Becker,⁶ Steffen Ganschow ³, Holger Fritze ⁴ and Simone Sanna ^{1,2}

¹Institut für Theoretische Physik, Justus-Liebig-Universität Gießen, Heinrich-Buff-Ring 16, 35392 Gießen, Germany

²Center for Materials Research (ZfM/LaMa), Justus-Liebig-Universität Gießen, Heinrich-Buff-Ring 16, 35392 Gießen, Germany

³Leibniz-Institut für Kristallzüchtung, Max-Born-Str. 2, 12489 Berlin, Germany

⁴Institut für Energieforschung und Physikalische Technologien, Technische Universität Clausthal, Am Stollen 19B, 38640 Goslar, Germany

⁵Institut für Metallurgie, Technische Universität Clausthal, 38678 Clausthal-Zellerfeld, Germany

⁶Institut für Physikalische und Theoretische Chemie, Technische Universität Braunschweig, 38106 Braunschweig, Germany



(Received 4 January 2024; revised 11 March 2024; accepted 15 April 2024; published 7 May 2024)

The ferroelectric to paraelectric phase transition in LiTaO₃ and in pure as well as Mg-doped LiNbO₃ is investigated theoretically by atomistic calculations in the framework of the density functional theory, as well as experimentally by calorimetry and electrical conductivity measurements. First-principles models within the stochastic self-consistent harmonic approximation (SSCHA) allow to consider anharmonic effects and thus to obtain a realistic estimate of the Curie temperature T_C of both ferroelectrics. *Ab initio* molecular dynamics (AIMD) calculations performed on large supercells confirm the Curie temperatures estimated with the SSCHA approach. Moreover, they also suggest that the structural phase transition is a continuous process beginning at temperatures well below T_C . According to AIMD, significant ionic displacements occur already at temperatures of about 100 K and 300 K below T_C in LiTaO₃ and LiNbO₃, respectively. To assess whether and how far the ionic displacements affect the materials properties, the AIMD results are compared with measurements of the electrical conductivity and of the heat capacity across the phase transition. Our first-principles calculations moreover show that Mg ions, a frequently employed dopant, raise the Curie temperature in LiNbO₃.

DOI: [10.1103/PhysRevMaterials.8.054406](https://doi.org/10.1103/PhysRevMaterials.8.054406)

I. INTRODUCTION

Lithium niobate (LiNbO₃, LN) and lithium tantalate (LiTaO₃, LT) are two isomorph ferroelectrics, which are among the most widely used electro-optic materials [1]. LN is characterized by unusually large pyroelectric, piezoelectric, electro-optic, and photo-elastic coefficients [1]. The magnitude of these coefficients is less pronounced in LT, which features, however, higher thermal stability. As an example, at high temperatures LT exhibits a much lower increase in electrical conductivity than LN, when the oxygen partial pressure is decreased [2]. Lithium niobate and tantalate are birefringent, have useful acoustic wave properties [3], and a rather large acousto-optic figure-of-merit. The wealth of physical effects and, more important, their magnitude, render LN and LT ideal candidates for acoustic and optical applications, exploiting both their bulk and surface properties [4].

Despite this wide range of applications, many aspects of the physics underlying the properties of LN and LT are not fully understood. This is particularly true for the phase transition between the paraelectric and the ferroelectric phases of the materials. This lack of knowledge is problematic. From an academic point of view, phase transitions are a fascinating topic, which deserves an accurate investigation. Moreover, the investigation of the ferroelectric to paraelectric transition is

of technological relevance. Indeed, devices such as sensors, are often operated at high temperatures, even close to the transition temperature.

The ferroelectric to paraelectric structural transition in LiNbO₃ and LiTaO₃ is a phase transition of the second order [5,6] according to the Ehrenfest notation. Accordingly, the spontaneous polarization P_S steadily grows with decreasing temperature from 0 to a value of 71(62) $\mu\text{C}/\text{cm}^2$ and 60(55) $\mu\text{C}/\text{cm}^2$ for congruent (nearly stoichiometric) LiNbO₃ [7] and LiTaO₃ [8], respectively. The onset temperature is known as transition or Curie temperature T_C , and has been measured to be in the range 1413 K (1140 °C)–1475 K (1202 °C) for LiNbO₃ [7,9] and in the range 874 K (601 °C)–958 K (685 °C) for LiTaO₃ [8,10], respectively. The large scattering of the measured values is in part due to the intrinsic difficulty to perform measurements at about 1500 K and in part to the nature of the phase transition, which is not a singular event occurring at T_C but rather a continuous transition taking place in a temperature interval around T_C [11,12].

It has been controversially discussed whether the transition is of displacive or order-disorder type. A typical signature of displacive transitions is the presence of one or more optical phonon modes, which become soft close to the Curie temperature T_C . No soft modes exist in order-disorder transitions, instead. Therefore, many different studies have been focused on the investigation of the phonon modes of LN [13–16] and LT [13,17–19]. Some of the investigations, including Rayleigh scattering, Raman spectroscopy, and infrared reflectivity, demonstrated the existence of a $A_1(\text{TO})$ optical phonon

*Corresponding author: felix.bernhardt@theo.physik.uni-giessen.de

becoming soft at high temperatures, suggesting a displacive nature of the transition [20–22]. This interpretation was corroborated by Wood *et al.*, who measured the birefringence of lithium niobate tantalate crystals ($\text{LiNb}_{1-x}\text{Ta}_x\text{O}_3$) for various compositions and temperatures, finding that it changes continuously across the Curie temperature, as expected for a displacive-type transition [23]. Yet, no mode softening could be observed in other studies, including neutron and Raman scattering experiments, suggesting the order-disorder nature of the ferroelectric to paraelectric phase transition [24–26]. Theoretical investigations based on the modeling of the phonon modes within the frozen phonon approach supported an order-disorder model for the oxygen atoms as the driving mechanism for the ferroelectric instability [27,28].

This apparent contradiction was solved later by *ab initio* [11] and classic [12] molecular dynamics simulations, which showed that the ferroelectric to paraelectric phase transition is (at least in LiNbO_3) of both order-disorder and displacive type. More in detail, the calculations demonstrated that the structural transformation is a process involving a displacive transition of the Nb sublattice and an order-disorder transition in the Li-O planes, which is completed at about T_C . Thus, the phase transition is a continuous process that takes place within a larger temperature interval and not an abrupt one as known, e.g., for solid to liquid structural transitions.

Although the contribution of the atomistic simulations has been crucial for the interpretation of the phase transition, the insight obtained in these studies must be considered of qualitative nature. *Ab initio* molecular dynamics simulations have been performed in smaller supercells [11], thus failing to accurately estimate the transition temperature. Finite-size effects indeed lead to the underestimation of T_C . Classic molecular dynamics can deal with larger supercells; however, they have limited predictive power. Calculations performed using different potentials predict a different behavior of the Nb sublattice below the Curie temperature [12,29]. Moreover, the theoretical investigations performed so far neglected the thermal expansion, which might be a problematic approximation for high values of T_C . For these reasons, the exact theoretical value of T_C for LiNbO_3 , LiTaO_3 and, more important, the temperature range in which the structural transformation occurs, are still to be determined.

An usual way to calculate the transition temperature from first principles is based on the estimate of the free energy of the two phases [30], with the vibrational contribution to the entropy accounted for in harmonic approximation. This procedure has been attempted also for LiNbO_3 and LiTaO_3 as well [17]. However, the presence of imaginary phonon modes in the paraelectric structure does not allow the accurate calculation of the transition temperature. Moreover, the harmonic approximation is questionable at temperatures close to T_C of the investigated system. A recent study pointed out the crucial role of anharmonicity in understanding the high temperature behavior, e.g., in thermal transport, of LT and, even more, of LN [31].

In this work, we employ two different approaches to investigate the behavior of LiNbO_3 and LiTaO_3 in the temperature interval enclosing the Curie temperature. On the one hand, we employ the stochastic self-consistent harmonic approach (SSCHA) for a realistic estimate of the transition temperature.

On the other hand, we perform *ab initio* molecular dynamics (AIMD) simulations on large supercells to estimate the temperature interval at which the structural transition occurs and investigate the mechanisms of the phase transition itself. We consider thereby the thermal expansion of the crystals. Both approaches can take anharmonicity into account and allow to investigate differences and similarities between LiNbO_3 and LiTaO_3 .

Calculations within the SSCHA approach yield a reliable phonon dispersion of the two phases and a realistic assessment of the transition temperature, which is calculated at 808 K for LiTaO_3 and at 1408 K for LiNbO_3 . AIMD models confirm that the phase transition is a complex process involving a displacive transition of the Nb ions with the oxygen octahedra at a temperature below T_C and an order-disorder transition in the Li ions, which is completed at T_C . In particular, substantial ion displacement is predicted at temperatures below T_C of about 100 K for LiTaO_3 and 300 K for LiNbO_3 . This temperature interval is further investigated by transport and calorimetry experiments. The measurements reveal modifications of the conductivity in a temperature range similar to the calculated interval, while the heat capacity continuously varies from the value of the ferroelectric phase to the value of the paraelectric phase in a more restricted interval.

It is moreover predicted that Mg doping, often used to enhance the resistance to optical damage, raises the transition temperature of stoichiometric LiNbO_3 . Density functional theory calculations within the nudged elastic band (NEB) method reveal that during the phase transition Mg has to overcome an energy barrier, which is at least an order of magnitude larger than for the Li atoms, thus locally pinning the ferroelectric phase. This confirms previous dielectric measurements of the Curie temperature as a function of the MgO content [32].

II. METHODOLOGY

A. Stochastic self-consistent harmonic approximation

For the accurate estimate of the Curie temperature, we calculate the free energy F per unit cell of the ferroelectric and of the paraelectric phase as a function of the temperature. The free energy per unit cell is given as

$$F = F_{\text{el.}} + F_{\text{phon.}} = U_{\text{el.}} + \sum_{\mathbf{q}, \nu} \left[\frac{1}{2} \hbar \omega(\mathbf{q}, \nu) + k_B T \ln \left(1 - \exp \left\{ \frac{-\hbar \omega(\mathbf{q}, \nu)}{k_B T} \right\} \right) \right] \quad (1)$$

where $\omega(\mathbf{q}, \nu)$ are the phononic frequencies of mode ν at \mathbf{q} -point \mathbf{q} . We note that the frequencies $\omega(\mathbf{q}, \nu)$ parametrically depend on the unit-cell volume, which is itself a function of temperature. Due to the large fundamental gap of LiTaO_3 and LiNbO_3 , the electronic entropy can be neglected in first approximation [33].

To estimate energies and frequencies in Eq. (1), the DFT as implemented in VASP [34–36] is employed. PAW potentials [37,38] with PBEsol exchange-correlation functional [39] and electronic configurations $1s^2 2s^1$, $4p^6 4d^3 5s^2$, $5s^2 5p^6 5d^3 6s^2$, and $2s^2 2p^4$ for Li, Nb, Ta, and O, respectively, are used.

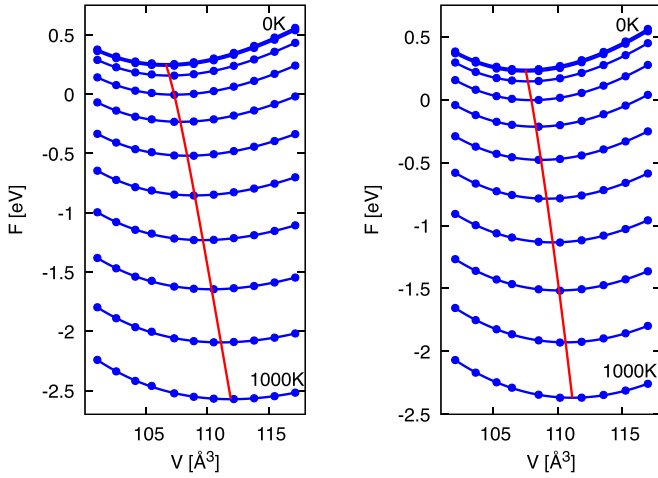


FIG. 1. Gibbs free energy for different temperatures vs unit-cell volume of LiTaO_3 . The left-hand side contains data from the ferroelectric phase, the right-hand side for the paraelectric phase. The datapoints are fitted to the Murnaghan-Birch equation of state, its minimum denotes the equilibrium volume at the corresponding temperature. The red line serves as a guide to the eye.

Our calculations include collinear spin polarization. Hubbard corrections according to the simplified approach proposed by Dudarev *et al.* [40] are applied to the d orbitals of Ta and Nb. Thereby we employ effective U values of $U_{\text{eff}} = 4$ eV for Nb and $U_{\text{eff}} = 5$ eV for Ta, according to Ref. [41]. Rhombohedral unit cells with $R3c$ and $R\bar{3}c$ symmetries model the ferroelectric and paraelectric phase of LN and LT, respectively. A $6 \times 6 \times 6$ Monkhorst-Pack K-point mesh [42], as well as an energy cutoff of 500 eV are needed to converge electronic energies to 10 meV. A Gaussian smearing with width 0.02 eV is applied to the Fermi occupancies. The ionic positions are optimized, such that all forces acting on the ions are lower than 0.005 eV/Å.

In order to obtain the unit-cell volume as a function of temperature, we employ the quasiharmonic approximation (QHA) as implemented in phonopy [43,44]. Following the procedure outlined in Ref. [45], we calculate harmonic phonon frequencies using the finite differences method with $3 \times 3 \times 3$ supercells at different volumina. Using the Parlinski-Li-Kawazoe method to interpolate the phonon frequencies to arbitrary q points [46], we obtain the harmonic phonon frequencies on a $20 \times 20 \times 20$ mesh. This yields phononic free energies converged within 1 meV with respect to a twice as dense q -point mesh. These frequencies and volumina are then used to calculate the Gibbs energy at different temperatures [assuming no internal pressure, see Eq. (2)]. Fitting the Gibbs energy via the Murnaghan-Birch equation of state, we obtain the equilibrium volume as a function of temperature. This is shown exemplarily for LiTaO_3 in Fig. 1 (also see the Supplemental Material, SM [47]),

$$G(T) = \min_V [U_{\text{el}}(V) + F_{\text{phon.}}(T; V)]. \quad (2)$$

Here, we consider rather high temperatures. It is therefore not reasonable to assume the validity of the harmonic approximation. Furthermore, the harmonic phonon frequency spectrum of the paraelectric (PE) phase of LT contains imagi-

nary modes [17]. An approach beyond the harmonic estimate of the phonon frequencies, which includes thermal fluctuations, is needed.

Thermal fluctuations (in particular anharmonic fluctuations) are often neglected in atomistic calculations. However, they affect the atomic structure, the phonon spectrum and thus the free energy of crystalline solids. The stochastic self-consistent harmonic approximation (SSCHA) method is an approach that allows to perform crystal geometry relaxation on the quantum mechanically calculated free-energy landscape, optimizing the free energy with respect to all degrees of freedom of the crystal structure [48]. In order to account for nuclear thermal fluctuations, however, the full Born-Oppenheimer energy surface, as well as its derivatives with respect to ionic positions (forces) and cell parameters (stress tensor) must be known, i.e., they must be calculated, e.g., by DFT within the stochastic approach as described in the following. Within this approach, we get access to the thermodynamics of crystals accounting for nuclear thermal anharmonic fluctuations.

We use the SSCHA [49–52] as implemented in `python-sscha` [48] to include anharmonic phononic effects. The formalism being used is described in detail in Ref. [48]. We adopt the nomenclature established therein.

In a first step, to sample the free-energy landscape, a set of random ionic configurations is created in a chosen supercell according to the Gaussian probability distribution for the ions. Due to the severe computational cost, we only calculate anharmonic effects for selected temperatures using $2 \times 2 \times 2$ supercells (80 atoms). The equilibrium volume at a given temperature is assumed to be the one calculated within the QHA.

For paraelectric (PE) LT and LN, we generate up to 400 structures per ensemble (see the SM [53]). As ferroelectric (FE) LT and LN have a lower symmetry, a larger ensemble size is necessary. Here, we use up to five times as many structures as for paraelectric LT or LN. On average, four ensembles are needed to find the free energy minimum. Lastly, another ensemble is created to calculate the anharmonic phonon frequencies. This last ensemble includes 10000 structures, in order to achieve convergence of the phonon frequencies of around 5 cm^{-1} , compared to a twice as large ensemble size. We assume the so called bubble approximation (see Ref. [48]), as its first-order correction has only a minimal effect on the phonon frequencies. Again, these frequencies are then interpolated onto a $20 \times 20 \times 20$ mesh (see the SM [54]).

The electronic energy is calculated using a stochastic average over this last ensemble, where the electronic energy of each structure is weighted according to the given temperature and dynamical matrix. The resulting stochastic uncertainty of the electronic energies is less than 1 meV.

Finally, inserting the calculated anharmonic phonon frequencies and electronic energies into Eq. (1), we can compare the free energy of both phases as a function of temperature.

B. Molecular dynamics

While standard DFT calculations model atomic systems at 0 K, molecular dynamics runs allow to model atomic structures at finite temperatures by coupling the system with a

thermostat. The latter initializes the velocities of the atoms according to the Maxwell-Boltzmann distribution at the considered temperature. The time evolution of the system is obtained by solving the Newton equation of motion by means of a Verlet algorithm within a given time step. At each time step, the forces acting on the ions are calculated within quantum mechanics. In our calculations, we employ a time step of 2 fs and model the time evolution for about 5 ps. The first 1 ps of the MD trajectories, in which the system reaches thermal equilibrium is discarded and not considered for the data analysis. For the calculations of the MD trajectories, the Nosé-Hoover thermostat [55,56] is employed, which models a canonical NVT ensemble.

AIMD calculations are performed within the numerical approach described in the previous section, i.e., the DFT as implemented in VASP [34–36], in combination with PAW potentials [37,38] and the PBEsol [39] exchange-correlation potential is employed. The wave functions are expanded in a plane wave basis up to 400 eV. In order to avoid self-correlation effects due to the periodic boundary conditions, very large supercells consisting of a $4 \times 4 \times 4$ repetition of the rhombohedral unit cell (640 atoms) are employed. Accordingly, the volume of the Brillouin zone is rather limited and the energy integration is performed at the zone center (Γ point). The volume of the cells in real space is calculated within the QHA at each considered temperature, as described in the previous section. Test calculations reveal that neglecting the thermal expansion and using supercell of smaller size lead to results that are qualitatively similar. However, a serious underestimation of the transition temperature occurs as discussed in the next section.

From the AIMD runs a real-time polarization can be extrapolated. Strictly speaking, the macroscopic polarization P_S for a supercell must be calculated within the modern theory of polarization as a Berry phase of the Bloch orbitals [57–59]. Yet, this approach is time consuming and cannot be applied to thousands of configurations of supercells containing 640 atoms. We employ, therefore, a simplified, approximated approach, in which the macroscopic polarization is defined as dipole moment per volume unit calculated with respect to a reference phase with $P_S = 0$ (e.g., the paraelectric phase) (see the SM [60]).

C. Sample growth and calorimetry

A LiTaO₃ crystal was grown via induction heating using the Czochralski process. The process was carried out in a protective argon atmosphere with a small addition of oxygen (less than 1 vol %). The starting materials were mixtures of lithium carbonate (Li₂CO₃, Alfa Aesar, 5N) and tantalum pentoxide (Ta₂O₅, Fox Chemicals, 4N). The crystal was grown along the c axis at a 0.5 mm/h rate. Samples cut from the grown material are labeled by IKZ in the following. For comparison, a commercial lithium tantalate (LT) sample was utilized in this study. A wafer of congruent composition was purchased from Precision MicroOptics Inc. (PMO, USA) and was cut into wafers of dimensions $6 \times 5 \times 0.5$ mm³, with both X-cut and Z-cut orientations. Samples cut from the commercial wafer are labeled by PMO in the following. Lithium niobate (LN)

purchased from the same company and cut in the same state as LT was also employed in this research.

Differential scanning calorimetry (DSC) was applied to determine T_c . Thereby, a NETZSCH STA 449C “F3” thermal analyzer was used. Following the ASTM E1269 standard, three consecutive measurements were done under identical conditions with empty crucibles (reference and sample), Al₂O₃ powder as standard with known $c_p(T)$ values, and the powdered sample. Four subsequent measurements were conducted up to 1463 K in a flow mixture of 40 ml/min Ar and 20 ml/min O₂, with isothermal sections for equilibration. Subsequently, these heating segments’ $c_p(T)$ functions from the last three measurements were averaged and used for further evaluation.

D. Conductivity

To measure the electrical conductivity of LiNbO₃ and LiTaO₃ single crystals, platinum electrodes are deposited on the samples through screen printing. The thickness of the electrodes is around 3 μm. Subsequently, the pieces are annealed at 1000 °C for about an hour with a 2 K/min heating rate.

AC impedance spectroscopy is performed within a frequency range 1 Hz–1 MHz with an excitation AC voltage of 50 mV to measure the conductivity. An impedance/gain-phase analyzer (Solartron 1260, Ametek Scientific Instruments, Hampshire, UK) is used for this purpose. The measurements are carried out in air, in a tube furnace that can heat up to 1580 K at atmospheric pressure, starting from room temperature with a heating rate of 1 K/min. Precise temperature control is maintained using a Type S thermocouple to measure sample temperature and a Pt100 thermoresistor to compensate for cold-end temperature variations of the thermocouple.

Modeling the electrical properties of the samples was done using a single equivalent circuit consisting of a bulk resistor (R_B) in parallel with a constant phase element (CPE) based on the obtained single semicircular EIS features. The bulk conductivity σ is calculated using the formula $\sigma = t(AR_B)^{-1}$, where t and A represent the sample thickness and electrode area, respectively.

The activation energy E_A is determined using the Arrhenius relation as follows:

$$\sigma = \sigma_0/T \exp(-E_A/(k_B T)). \quad (3)$$

Here, σ_0 , k_B , and T represent a constant pre-exponential coefficient, the Boltzmann constant, and the absolute temperature, respectively. The Nernst-Einstein relation states that $1/T$ reflects the connection between mobility, which affects electrical conductivity, and thermally activated diffusion. Equation (3) provides the activation energy E_A if a single conduction mechanism dominates over an extensive temperature range, reflected by a constant slope in the Arrhenius representation. The logarithmic slope of σT in Eq. (4) is used for analysis as the Arrhenius plot does not show differences in electrical conductivity at high temperatures (more details on the procedure can be found, e.g., in Ref. [41]),

$$E_{\sigma T} = -k_B \frac{\partial \ln(\sigma T)}{\partial (1/T)}. \quad (4)$$

The consideration of σT is discussed in the following.

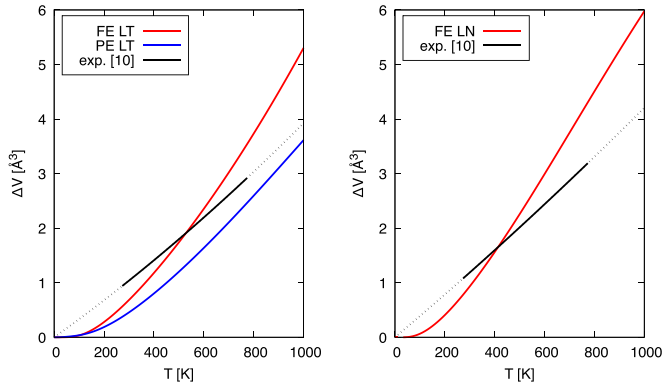


FIG. 2. Unit-cell volume expansion as a function of temperature for LiTaO₃ (left) and LiNbO₃ (right). The red and blue lines denote the thermal expansion of the ferro- and paraelectric configuration as calculated within the QHA, respectively. The black line is a measurement performed in reference [10].

III. RESULTS

A. Transition temperature

The Curie temperature of the structural transition between the ferroelectric and the paraelectric phase is obtained inserting the phonon frequencies including anharmonic contributions as estimated in the SSCHA framework and the

electronic energies into Eq. (1). The data are calculated considering the thermal expansion as estimated within the QHA, as shown in Fig. 2. The calculated data are in overall good agreement with the measured expansion of LiTaO₃ and LiNbO₃ as given by the coefficients from Ref. [10]. The calculated values slightly overestimate the measured volumes in both materials by around 2%, as known from GGA based exchange and correlation functionals. The deviations might also be related to the stoichiometric composition of the measured samples or by anharmonic contributions disregarded in the QHA.

Figure 3 shows the free energy of the unit cell of the ferroelectric and paraelectric structure of LT (top row) and LN (bottom row) as a function of the temperature. Electronic and vibrational contributions [as calculated with Eq. (1)] are shown in 3(a) and 3(b), respectively, while 3(c) shows the total free energy. Assuming a minor dependence on the pressure (a reasonable approximation for solids), the ground-state configuration for a certain volume is given at each temperature by the structure with the lower free energy. The Curie temperature is the intersection of both curves. In our calculation the intersection occurs at around 808 K and 1408 K for LiTaO₃ and LiNbO₃, respectively. They are rather close to the experimentally determined value of 874 K [8,10] and 1413 K [7], respectively, although the value calculated for LT underestimates somehow the measured value.

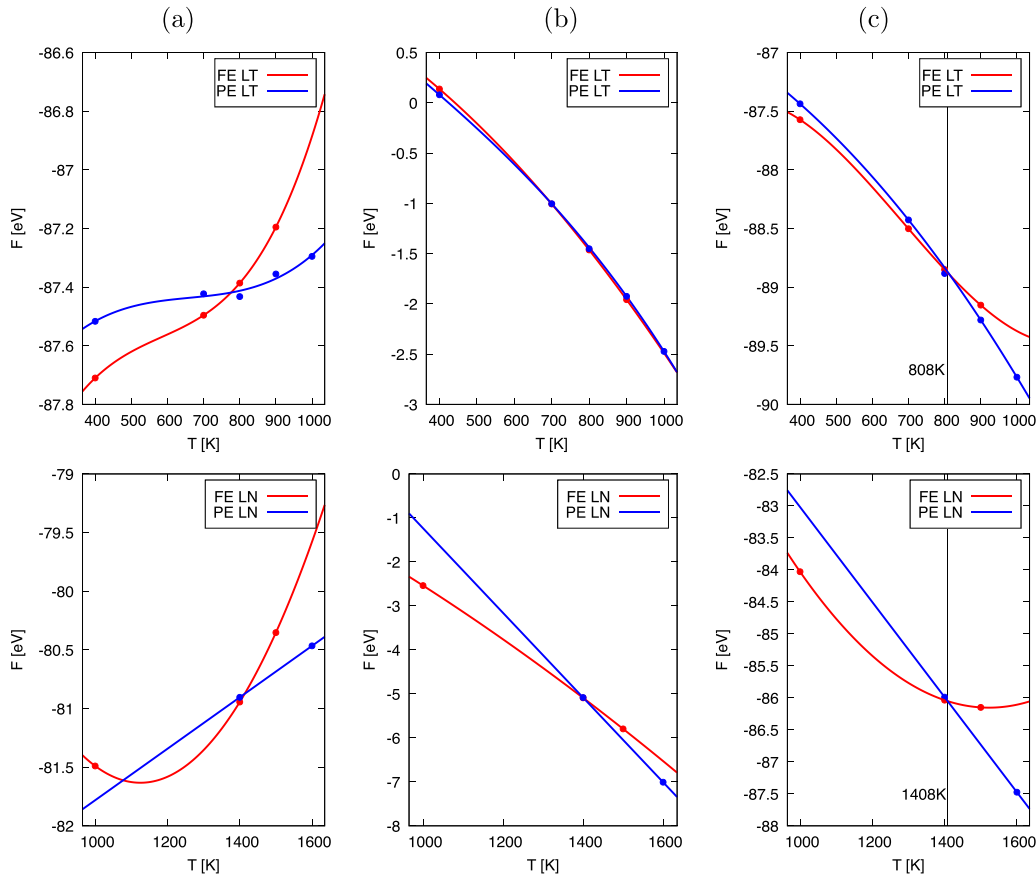


FIG. 3. Free energy per unit cell calculated as a function of the temperature for LiTaO₃ (top row) and LiNbO₃ (bottom row). The red and blue lines denote the free energy of the FE- and PE configuration as calculated within the SSCHA, respectively. (a) Electronic contribution, (b) vibrational contribution, and (c) total free energy are shown.

The transition temperature of LiNbO_3 was estimated in Ref. [17] comparing the free energies of the paraelectric and ferroelectric phases, similarly to the approach we apply, however, within the harmonic approximation. The calculated transition temperature was estimated to be 1000 K using the DFT calculated equilibrium volume and 1160 K using the high-temperature experimental volume. Our calculations based on the SSCHA formalism predict for LiNbO_3 a transition temperature of 1408 K and thus confirm not only the obvious consideration that quasiharmonic contribution are of fundamental importance, but also allow to quantify their impact on the overall results. Comparing the results obtained neglecting and including non-harmonic effects, we can conclude that they cause a shift of the transition temperature of ca. 250 K, greatly improving the agreement between measured and calculated transition temperatures.

B. Transition dynamics

After determining the Curie temperatures for the ferroelectric to paraelectric transition in LiTaO_3 and LiNbO_3 within the SSCHA approach, we adopt a microscopic perspective to investigate the atomic displacements at the phase transition. This yields information about the mechanisms of the phase transition at the atomic scale and about the width of the temperature interval at which the structural transition occurs.

In order to understand the atomic displacement at the structural transformation, it is crucial to describe the microscopic structure of the two phases involved in the transition. LiTaO_3 and LiNbO_3 can be both thought of as oxygen octahedra piled along the crystal c axis. These octahedra may be empty or host Li and Ta/Nb atoms. In the ferroelectric structure, the octahedra occupation follows the order (from bottom to top) Li, Ta/Nb, empty, Li, Ta/Nb, empty, and so forth, as shown in Fig. 4. The Nb/Ta atoms are not at the center of the oxygen octahedra, while the Li atoms are just above (or below) an oxygen plane. This atomic arrangement is noncentrosymmetric (space group $R3c$). The center of mass of the positive (Nb^{5+} , Ta^{5+} , Li^+) and negative (O^{2-}) charges are displaced, giving rise to a spontaneous polarization along the c axis as large as 0.60 C/m^2 for LiTaO_3 [8] and 0.71 C/m^2 for LiNbO_3 [7], as discussed in the introduction.

The high-temperature phase of LiTaO_3 and LiNbO_3 (above 874 K [8] and 1411 K [7], respectively) is paraelectric and belongs to the space group $R3c$. According to the general understanding of this structure, the Li ions lie exactly within the oxygen planes, while the Ta and Nb atoms sit exactly at the center of oxygen octahedra, as shown in Fig. 4. The structure has a higher symmetry than the ferroelectric phase. In particular, the centers of mass of the positive and negative charges coincide, and the crystal shows no spontaneous polarization. We remark that this picture has been previously questioned [11]. It has been suggested that it only holds in time average, while the instantaneous configuration features Li ions randomly distributed above or below the oxygen planes, so that oppositely directed microscopic dipole moments sum up to a zero net polarization [11].

The deviation of the atomic positions in the ferroelectric and paraelectric structure can be quantified by the displacement of the Nb/Ta ions from the oxygen cage center (ΔNb ,

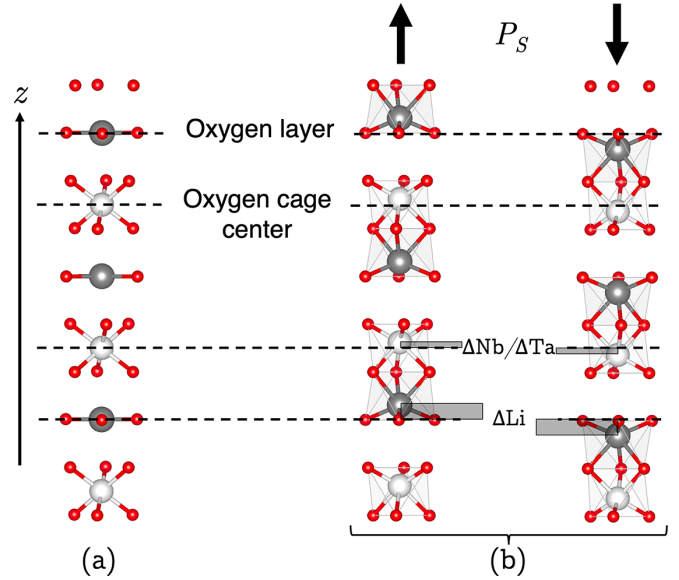


FIG. 4. Atomic structure of the (a) paraelectric and (b) ferroelectric phase of LiNbO_3 and LiTaO_3 . Nb/Ta atoms are white, Li atoms gray and O atoms red. The displacement from the atomic positions in the paraelectric phase is indicated with ΔNb or ΔTa and ΔLi , respectively. Both displacements occur in the crystallographic z direction, parallel to the spontaneous polarization P_S .

ΔTa) and of the Li ions from the oxygen planes (ΔLi). According to our calculations, at 0 K (in the ferroelectric phase) the displacements assume the value $\Delta\text{Nb} = 0.279 \text{ \AA}$, $\Delta\text{Li} = 0.717 \text{ \AA}$ in LiNbO_3 , and $\Delta\text{Ta} = 0.188 \text{ \AA}$, $\Delta\text{Li} = 0.643 \text{ \AA}$ in LiTaO_3 , respectively.

To investigate the dynamics of the phase transition, we estimate the temperature dependence of the parameters ΔLi and ΔNb , ΔTa , which we extract from the AIMD runs performed at different temperatures. Let us start our discussion with LiTaO_3 . From the crystal structure shown in Fig. 4, it can be expected that above the Curie temperature ΔLi and ΔTa are distributed about a value of zero, while at low temperatures they are distributed around the value calculated for 0 K of 0.188 \AA for ΔTa and 0.643 \AA for ΔLi , respectively.

In Fig. 5 the distributions of ΔLi (left) and ΔTa (right) extracted from AIMD runs of LiTaO_3 at different temperatures are shown (see the SM [61]). The distribution ΔLi and ΔTa well below T_C (e.g., at 300 K, black curve) are indeed centered at the expected values. The form of the distribution is Gaussian, as expected for the thermal broadening of the sharp peak of the ideal, rigid ferroelectric structure. In particular, we observe that the ΔLi probability distribution is unimodal, suggesting that all the Li ions are above the oxygen planes, as expected for the ferroelectric phase.

Figure 5(b) shows the probability distribution of ΔTa at different temperatures (Gaussian fit). The distribution is unimodal at each investigated temperature, as expected for a displacive transition. With increasing temperature, the distribution broadens, since the atoms vibrate with larger amplitude about the equilibrium positions. Moreover, the distribution smoothly moves toward $\Delta\text{Ta} = 0$. This can be interpreted as a consequence of the fact that Ta atoms can move relatively

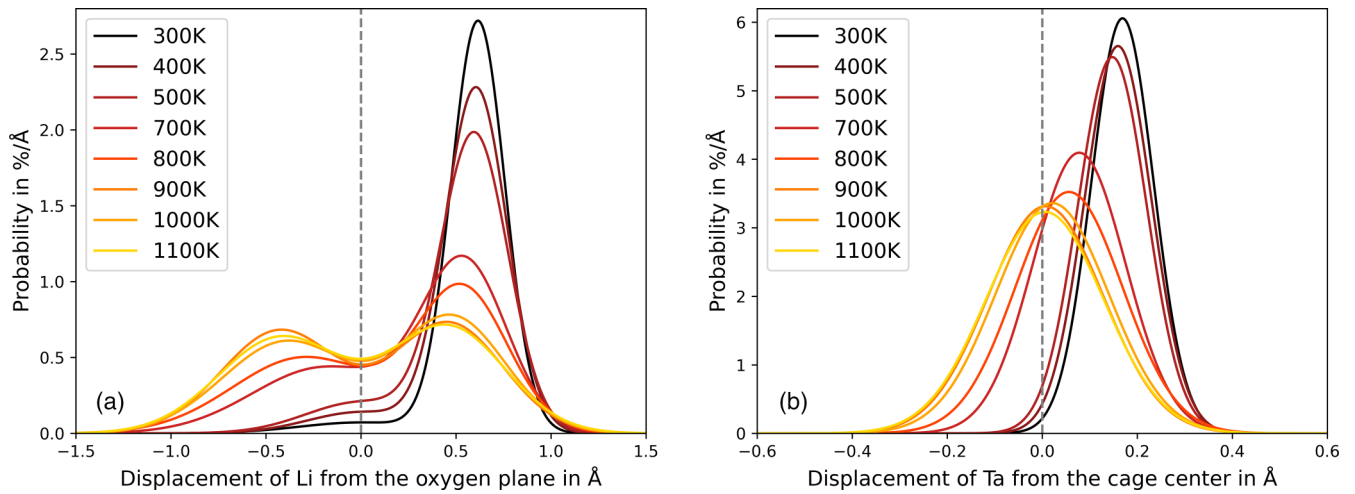


FIG. 5. (a) Temperature-dependent probability distribution of the parameter ΔLi (representing the displacement of the Li ions from the oxygen planes) for LiTaO_3 . The unimodal distribution well below the Curie temperature (e.g., at 300 K) means that all the Li ions are located above the oxygen planes. The symmetric, bimodal curve at above the Curie temperature (e.g., at 1100 K) indicates that the Li ions are randomly distributed above or under the oxygen planes, as expected for an order-disorder phase transition. (b) Probability distribution of the parameter ΔTa (representing the displacement of the Ta ions from the center of the oxygen octahedra). The distribution is unimodal at every temperature, as expected for a displacive phase transition.

free within the oxygen octahedra, as they do not need to overcome any energy barrier to move from the ferroelectric to the paraelectric configuration.

The temperature dependence of the probability distribution of ΔLi , shown in Fig. 5(a) is in striking contrast with the probability distribution of ΔTa . With growing temperatures, the distribution does not substantially shift toward $\Delta\text{Li} = 0$. Instead, it becomes bimodal. Well above the structural transition, the distribution is symmetric with respect to $\Delta\text{Li} = 0$ (oxygen lattice plane), which represents a local minimum. Only a small fraction of the Li atoms lies exactly in the plane, independently from the temperature. While the oxygen plane has been regarded as an energetic barrier (at least for LiNbO_3) in the past [12], it can also be stated that when the Li atoms oscillate around $\Delta\text{Li} = 0$ their velocity is maximal and their probability to be found at this point is minimal.

The calculated curves shown in Fig. 5(b) demonstrate that for temperatures well below T_C almost all Li atoms are distributed about the positions they assume in the ferroelectric structure. With increasing temperature a growing fraction of Li atoms possesses enough thermal energy to pass the oxygen plane. Above T_C all Li atoms have sufficient energy to move across the oxygen plane, so that they are distributed roughly with the same probability above or below an oxygen plane. The sum of all Li contributions to the spontaneous polarization vanishes. However, P_S is exactly zero only in average, as each unit cell still has a finite, randomly distributed, dipole moment. This feature is compatible with an order-disorder type structural transition. This is in agreement with a recent x-ray diffraction investigation showing that ordering of the disordered Li ion in the polar direction accompanied by deformation of the oxygen octahedra leads to the ferroelectric phase transition [62].

We observe that already at temperatures significantly lower than T_C the probability distributions for both ΔLi and ΔTa (e.g., already at 700 K) substantially differ from the distri-

butions calculated for low temperatures (e.g., 300 K). This suggests that the phase transition does not occur abruptly at a given temperature, but is rather a continuous process, occurring dynamically over a certain range of temperatures. The width of this temperature range will be explored in the next sections.

The instantaneous spontaneous polarization can be extrapolated from the AIMD snapshots with the simplified approach explained in the methodological section. The average polarization of LiTaO_3 as a function of the temperature is shown in Fig. 6(a). The calculated data can be fitted by a root function. The critical exponent of the order parameter in a mean-field theory such as the Landau-Ginzburg theory is 0.5; however, lower exponents are calculated within other approaches. In this work, we chose a square root fit of the spontaneous polarization as a function of the temperature, as expected for a second-order phase transition in the Landau-Ginzburg theory. The square root function equals zero at 841 K. At this temperature, the polarization vanishes and the crystal is in the paraelectric configuration. This value is in excellent agreement with the experimentally determined transition temperature of 873–878 K [8,63,64].

The contribution to the polarization of the different species is also shown in Fig. 6(a). It can be observed that both the Li and Ta contribution are roughly a square root function of the temperature. The Ta atoms, which experience limited shifts but carry a high (nominal) charge of 5+ electrons, have a larger contribution to the total polarization than the Li atoms, which undergo larger displacements but carry a much lower (nominal) charge of 1+ electrons.

Summarizing, the AIMD calculations reveal that the ferroelectric to paraelectric transition in LiTaO_3 is a dynamical process of displacive type in the Ta sublattice and of order-disorder type in the Li sublattice. The square root fit of the spontaneous polarization vanishes at 841 K, which can

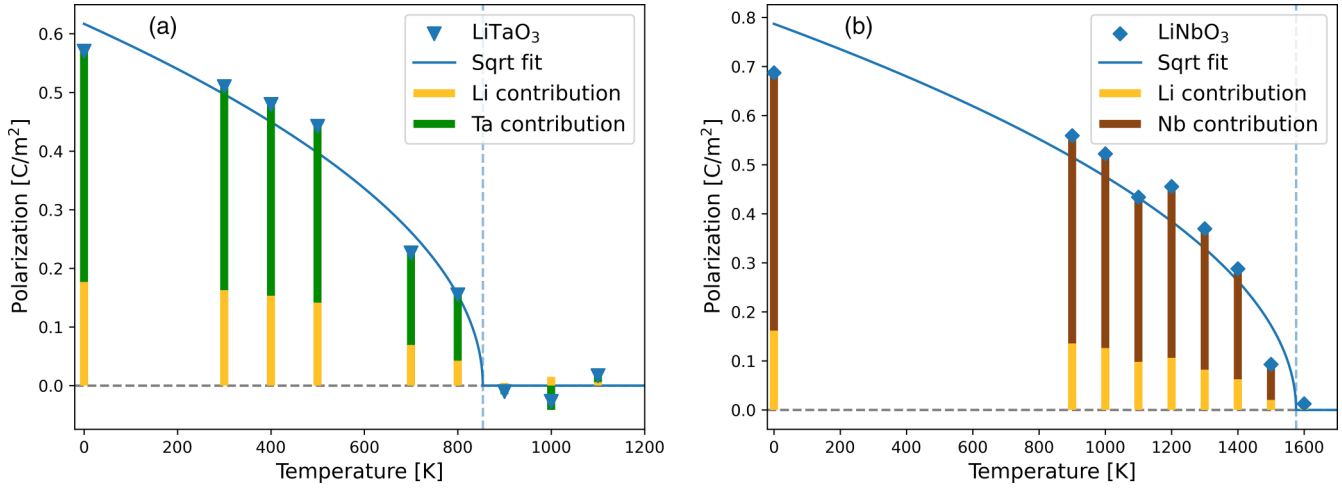


FIG. 6. Calculated temperature dependence of the spontaneous polarization P_3 for (a) LiTaO_3 and (b) LiNbO_3 . The solid line is a square root fit of the calculated data, represented by the histograms. The latter are color coded according to the contribution of the Li sublattice (in yellow) and of the Ta/Nb sublattice (green/brown).

be considered as the T_C value predicted by AIMD. A similar behavior has been previously proposed for LiNbO_3 [11,12].

Figure 7 shows the temperature-dependent probability distribution for ΔLi and ΔNb for LiNbO_3 extrapolated from the AIMD trajectories. The overall behavior is qualitatively similar to LiTaO_3 . The distributions can be fitted by one (Nb) or two (Li) Gaussian curves, with the distribution ΔNb unimodal for all investigated temperatures. The distribution of ΔLi is bimodal and again symmetric with respect to the oxygen plane in the paraelectric configuration, and unimodal at low temperatures. As the relevant temperatures in LiNbO_3 are higher than in LiTaO_3 , the Gaussian distributions are broader. We point out that caution is due in the interpretation of the displacement distribution at 1600 K in Fig. 7, as this temperature is beyond the melting point of LiNbO_3 . Due to known deficiencies of

MD in the estimation of the nucleation free energy barrier between the solid and the liquid phases [65], the material is modelled at this temperature as an overheated phase.

The spontaneous polarization, shown in Fig. 6(b), is fitted by a square root function, which vanishes at 1524 K, which slightly overestimates the experimentally determined transition temperature of 1430–1475 K [7,63,64]. Again, the Li sublattice has a smaller contribution to the spontaneous polarization than the Nb sublattice. Considering the thermal expansion is fundamental for a realistic estimate of the transition temperature (see the SM [66]).

Our calculations for LiNbO_3 confirm the suggestion first made in [11,12] that the phase transition is of mixed displacive and order-disorder type, as it involves a displacive transition of the Nb ions within the oxygen octahedra and an order-disorder

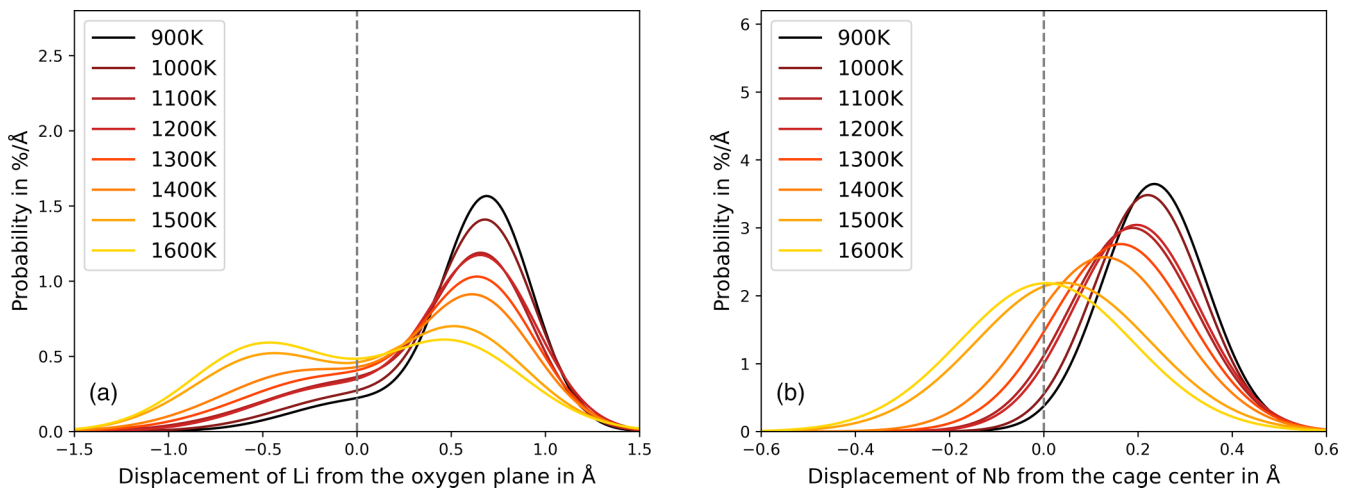


FIG. 7. (a) Temperature dependent probability distribution of the parameter ΔLi (representing the displacement of the Li ions from the oxygen planes) for LiNbO_3 . The unimodal distribution well below the Curie temperature (e.g., at 900 K) means that all the Li ions are located above the oxygen planes. The symmetric, bimodal curve at above the Curie temperature (e.g., at 1600 K) indicates that the Li ions are randomly distributed above or under the oxygen planes, as expected for an order-disorder phase transition. (b) Probability distribution of the parameter ΔNb (representing the displacement of the Nb ions from the center of the oxygen octahedra). The distribution is unimodal at every temperature, as expected for a displacive phase transition.

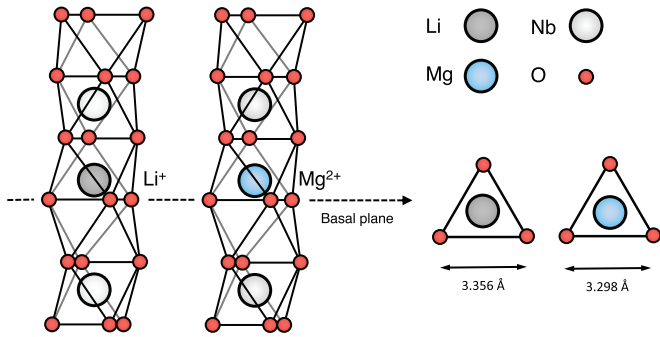


FIG. 8. Schematic representation of the atomic structure of undoped and Mg-doped LiNbO_3 . The oxygen-oxygen interatomic distances are given.

transition of the Li sublattice. The atomic structure and the spontaneous polarization change gradually between the ferroelectric and paraelectric phase, so that the transition does not occur abruptly at a well defined temperature but rather over a temperature range of several 100 K, which will be further investigated later.

C. Effect of Mg doping on the transition temperature

In a final step, we investigated how Mg doping affects the Curie temperature of LiNbO_3 . Mg is the chief dopant for LiNbO_3 , if the optical damage resistance has to be enhanced. Indeed, a concentration of Mg exceeding a so called threshold of about 5 mol% leads to a reduction of the optical damage of more than two orders of magnitude [6]. The mechanism leading to the optical resistance is quite indirect. The Mg incorporation leads to the formation of $\text{Mg}_{\text{Li}}^{2+}$ substitutionals [67], which inhibit the formation of Nb_{Li} antisites (small bound polarons) that are crucial for the photorefractivity. In LiTaO_3 , doping with Mg lowers the photorefraction as well [68]; however, we limit our investigation to LiNbO_3 .

Whether Mg increases or decreases T_C depends on the sample composition (nearly stoichiometric or congruent) and on the Mg concentration [69]. In our models, we consider a number of $\text{Mg}_{\text{Li}}^{2+}$ substitutionals in stoichiometric LN which corresponds to 5.56 mol%. This is a typical doping concentration of the LN samples used, e.g., for the fabrication of optical waveguides. As no experimental evidence of Mg clustering in LN is available, we assume a homogeneous distribution.

The position of Li^+ and Mg^{2+} within the oxygen octahedra is different. Although the distance to the three oxygen ions below them is roughly the same (2.013 Å and 2.022 Å for Li^+ and Mg^{2+} , respectively), the distance to the three oxygen ions above them is much shorter for Mg^{2+} (2.172 Å) than for Li^+ (2.291 Å). Thus, the oxygen octahedra occupied by the $\text{Mg}_{\text{Li}}^{2+}$ substitutional is more contracted than the octahedron occupied by a regular Li^+ ion. The contraction is also visible in the oxygen-oxygen interatomic distance, which is much shorter in the Mg^{2+} octahedron (3.298 Å vs 3.356 Å), as shown in Fig. 8. In this configuration, Mg doping does not induce localized defect states in the LiNbO_3 bandgap (see the SM [70]).

The AIMD runs of supercells containing Mg show the same qualitative trend as the supercells modeling the undoped

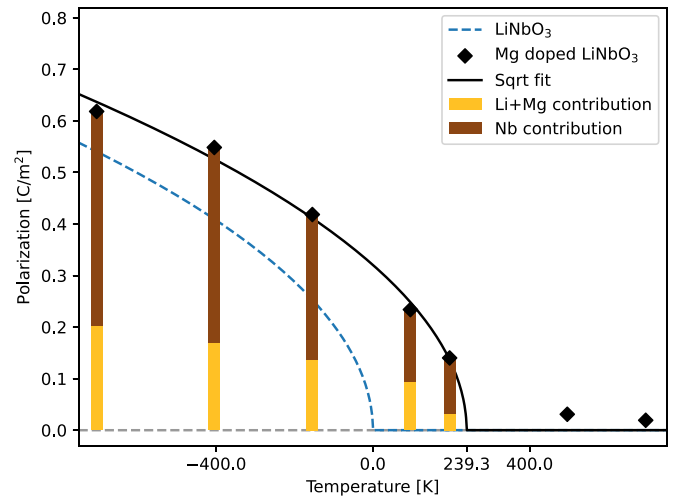


FIG. 9. Calculated temperature dependence of the spontaneous polarization P_S for Mg-doped (solid line) and undoped (dashed line) LiNbO_3 . The solid line is a square root fit of the calculated data, represented by the histograms. The temperature is given with respect to the calculated transition temperature of undoped LiNbO_3 .

material. The probability distributions of ΔLi and ΔNb have a similar form and temperature dependence as in the case of the undoped crystals; however, they are shifted to higher temperatures. Correspondingly, the spontaneous polarization vanishes at temperatures of about 240 K higher, as shown in Fig. 9. This value, which must be considered as a rough estimate, is in qualitative agreement with the experimental observation. For a doping of 1.2 atom %, a Curie temperature of 1493 °C is measured [71], which is 80 K higher than the value of 1413 °C measured for the undoped samples [7].

This effect can be explained by different factors. The Mg ions pin the polarization locally, as they require more energy than Li ions to pass the oxygen layer. The minimum energy path for the migration of the $\text{Mg}_{\text{Li}}^{2+}$ substitutional to the empty octahedron interstitial position has been calculated by the NEB method, considering six images between start and end configuration. Start and end configuration are shown in the inset of Fig. 10.

The calculated energy barrier of 0.47 eV is roughly an order of magnitude higher than the barrier that we calculate, e.g., for a similar migration path of Li in hydrogenated LiNbO_3 . The reason for such a striking difference of the barrier heights cannot be merely geometric, as Mg and Li have nearly identical ionic radii (0.90 Å for Li^+ and 0.86 Å for Mg^{2+} in octahedral coordination [72]). However, the position of the two ions within the oxygen octahedra is different. In particular, the oxygen octahedra occupied by the $\text{Mg}_{\text{Li}}^{2+}$ substitutional is more contracted than the octahedron occupied by a regular Li^+ ion, probably due to the larger Coulomb attraction between the cation and the anions. Thus, the oxygen ions in the basal plane that has to be crossed during the phase transition build a tighter mesh for Mg^{2+} (O-O distance 3.298 Å) than for Li^{2+} (O-O distance 3.356 Å), as shown in Fig. 8. We thus suggest that on the one hand a larger deformation of the oxygen octahedra, and on the other hand a stronger Mg-O

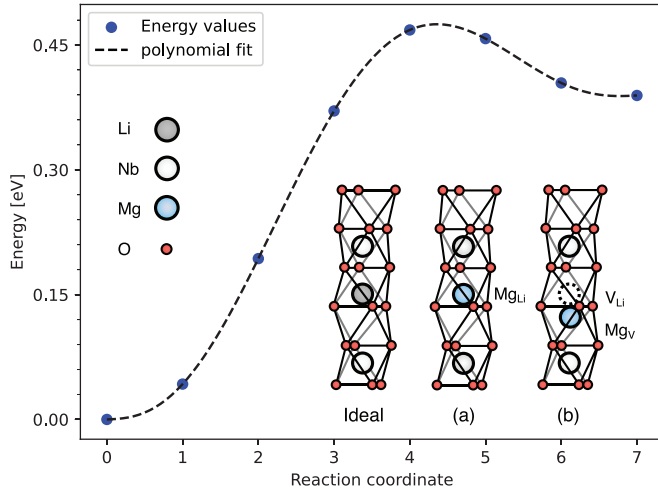


FIG. 10. Energy barrier associated with the $\text{Mg}_{\text{Li}}^{2+}$ diffusion to an empty octahedron, calculated for LiNbO_3 with the NEB method and six images besides start and end configuration. Dotted lines are polynomial fits of the calculated data. The inset shows the undoped crystal structure as well as start and end configuration of the NEB.

bond than the Li-O bond, both contribute to locally pin the polarization and thus the ferroelectric phase.

D. Comparison with experimental results

Although the calculated Curie temperatures reasonably match the experimental data, it becomes clear from the AIMD that the atomic positions start to shift at temperatures well below T_C . An interval of about 100 K and 300 K for LiTaO_3 and LiNbO_3 , respectively, can be identified, in which the largest part of the structural modifications occur.

In order to define more closely this interval, we compare the calculated value of the spontaneous polarization as well as the octahedra occupation with physical quantities that can be observed experimentally by characterizing the crystals across the phase transition. In the following, we start our discussion with LiTaO_3 , which is easier to characterize experimentally due to the lower T_C .

To characterize the phase transition, we define the occupation of the regular Li octahedra as a reaction coordinate. In the ferroelectric phase and at very low temperatures, the occupation of the regular Li octahedra is roughly 100%. For increasing temperature, the Li atoms may possess enough thermal energy to overcome the energy barrier represented by the oxygen plane and migrate into the vacant oxygen octahedra (see, e.g., Fig. 4). In the paraelectric phase, the Li atoms jump continuously between the Li octahedra and the vacant octahedra, resulting in an occupation of 50% of the regular Li octahedra. The occupation of the regular Li octahedra is shown in Fig. 11 (black triangles). The solid line is a fit of the calculated data by a sigmoid function (fits with other functions are possible as well), which only serves as a guide to the eye.

The interval at which the occupation of the Li octahedra changes from 100% to 50% is an estimate of the temperature interval at which the phase transition occurs. In the case of LT, the width of this interval is roughly 100 K.

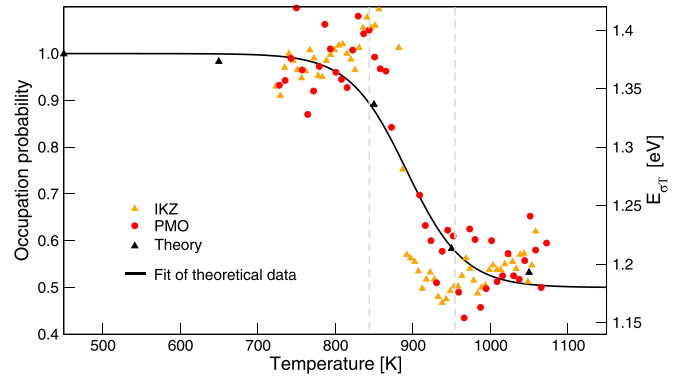


FIG. 11. Calculated temperature-dependent occupation of the regular Li octahedra (black triangles), fit through a sigmoid function (solid line) and measured slope of the electrical conductivity of LiTaO_3 . Note that the scatter of $E_{\sigma T}$ is caused by the calculation of the slope of the electrical conductivity using Eq. (4). For the sake of clarity, the calculated data is rigidly translated to match the measured T_C . The samples used for the measurements are named according to the description in the conductivity section.

It is known that the electrical conductivity of LT changes at the transition from the ferroelectric to the paraelectric phase, at which the measured activation energy decreases from a value of 1.38 eV to 1.19 eV [2]. Accurate experiments have been performed on different PMO samples (see Sec. II C) to explore the temperature range around T_C and establish whether the octahedra occupation correlates with the crystal conductivity. The corresponding measurements are shown in Fig. 11. The temperature interval at which the slope $E_{\sigma T}$ varies from 1.38 eV to 1.19 eV roughly corresponds to the theoretically predicted range, confirming that the phase transition is a continuous process extending over a larger temperature interval. The comparison between calculated and measured data also shows a correlation between octahedra occupation and conductivity. The analysis of this correlation is, however, beyond the scope of this paper and is discussed elsewhere [63]. Although the measurement clearly shows that the conductivity starts to change well below the Curie temperature, the scattering of the measured data (due to the calculation of the derivative of the conductivity) does not allow a more precise estimate of the interval width at which the transformation occurs.

For that reason, we correlate the measured conductivity with the spontaneous polarization as a function of the temperature, as shown in Fig. 12. Indeed, the order parameter has at least a well defined point at which it vanishes, namely T_C , which can be considered the end of the temperature interval at which the transition occurs. The starting point can be arbitrarily chosen to be the point at which the order parameter has grown to a factor $1/e$ of the 0 K value. This region is marked in gray in Fig. 12 and corresponds to about 100 K. Interestingly, the conductivity jumps roughly in this temperature range from the value of the paraelectric to the value of the ferroelectric phase. This confirms, again, that the geometry modification starts to affect the material properties below T_C .

Another thermodynamical quantity, which is expected to be affected by the phase transition is the heat capacity. As the

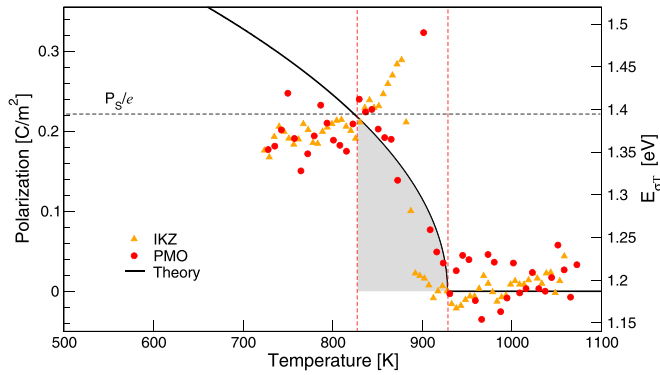


FIG. 12. Calculated spontaneous polarization as a function of the temperature (solid line) and measured slope of the electrical conductivity of LiTaO₃. For the sake of clarity, the calculated data is rigidly translated to match the measured T_C . The samples used for the measurements are named according to the conductivity section. The gray region marks the temperature interval at which the polarization has decreased below a factor $1/e$ of the 0 K value.

ferroelectric and the paraelectric phase have different symmetry, also the phonon population is different and with it the capacity of the material to store energy. In order to verify in which temperature range the thermal capacity of LiTaO₃ jumps from the value measured for the ferroelectric phase to the value measured for the paraelectric phase, calorimetry experiments have been performed. The corresponding measurements are shown in Fig. 13 and again compared with the theoretically predicted order parameter. The jump of C_p takes place in a temperature range, which is narrower than the range at which the octahedra occupation or the conductivity changes. The involved temperature range corresponds to the interval at which the spontaneous polarization grows from zero to a value roughly $1/2e$ smaller than the 0 K value. Thus, although the measurements corroborate the hypothesis that the structural transition is a continuous process affecting the materials properties already below T_C , the temperature

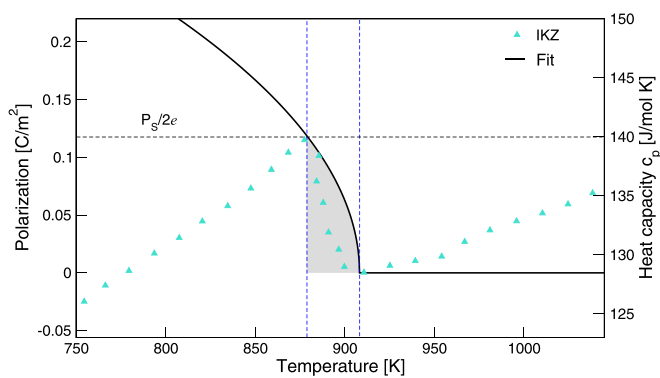


FIG. 13. Calculated temperature dependence of the spontaneous polarization (solid line) and measured thermal capacity at constant pressure C_p of LiTaO₃ (light blue triangles). For the sake of clarity, the calculated data is rigidly translated to match the measured T_C . The gray region marks the temperature interval at which the polarization has decreased below a factor $1/2e$ of the 0 K value.

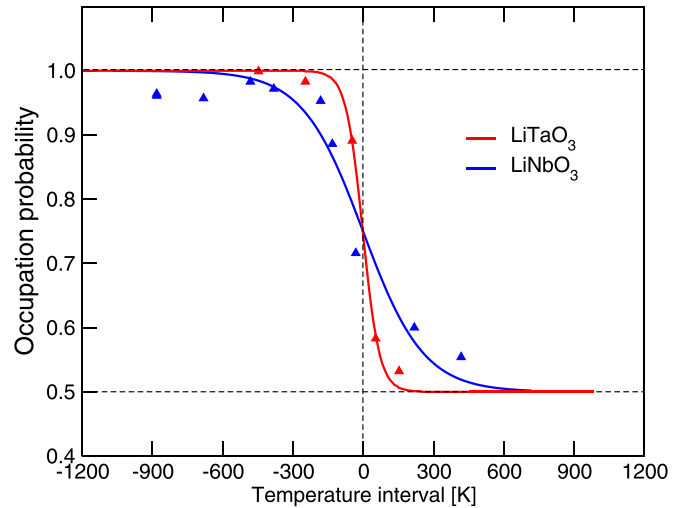


FIG. 14. Comparison of the calculated temperature dependence of the occupation of the regular Li octahedra in LiTaO₃ (red triangles) and LiNbO₃ (blue triangles). The solid line is a sigmoid function fit of the calculated data. The data is shifted, so that the inflection point of each curve is at the origin of the temperature axis.

interval depends on how the microscopic structure affects the measured quantity (see the SM [73]).

Also in the case of LiNbO₃ it becomes evident that similarly to LiTaO₃ the atomic displacements have an influence on the conductivity and on the heat capacity below T_C . Again, the temperature interval depends on the investigated property. Finally, the octahedra occupation of LiTaO₃ and LiNbO₃ as a function of temperature is compared. It might be supposed that the energy needed from the Li atoms to pass the oxygen plane is of the same order of magnitude in the two compounds. It is therefore reasonable to assume that the Li ions begin their migration at similar temperatures in the two crystals. However, as the Curie temperature of LN is much higher than the Curie temperature of LT, it is expected that the structural transition in LN occurs in a somewhat larger temperature interval. The AIMD trajectories confirm this hypothesis. Figure 14 shows the occupation of the Li octahedra for the two compounds. While in LT the occupation sinks from 100% to 50% within 100 K, in LN the same occurs within a substantially larger temperature range of about 300 K.

Finally, we remark that, besides doping, also the intrinsic defect structure will affect the ferroelectric phase transition in LiNbO₃ and LiTaO₃. In LiNbO₃, specific structural defects are known, that are likely to be formed [74,75]. In particular, a Nb_{Li} antisite that is charge compensated by four Li vacancies (Li vacancy model) is currently assumed to be the dominant defect cluster. In LiTaO₃, the defect structure is more complex, yet a Ta at an interstitial position and charge compensated by five Li vacancies has been identified as an energetic favorable structure [76]. The dipole moments associated with the defect clusters will locally affect the materials properties and locally pin the polarization. The diffusivity of the lithium vacancies is low at room temperature, which indicates that the defect complexes are rather stable. Even at high temperatures, although the Li vacancies become very mobile [77], the reported cohesive energy of above 4 eV of the

clusters [74] suggests that the clusters may still affect the transition temperature by locally pinning the crystal structure. The local pinning will result in an extension of the temperature range of the transition temperature. A quantitative analysis of this effect is beyond the goals of this investigation.

IV. SUMMARY AND OUTLOOK

The ferroelectric to paraelectric phase transition in LiTaO₃ and LiNbO₃ has been investigated theoretically and experimentally. First-principle calculations in the framework of the SSCHA formalism predict a transition temperature of 808 K and 1408 K, for LiTaO₃ and LiNbO₃, respectively, which are in rather good agreement with the measured values. AIMD calculations give insight into the mechanisms of the phase transition. The latter is a complex process, in which Li and Nb/Ta behave differently. The Li sublattice undergoes an order-disorder structural transition, while the Nb/Ta sublattice undergoes a displacive type transition. For both LiTaO₃ and LiNbO₃, substantial atomic displacements are predicted for temperatures smaller than T_C . From an atomistic perspective, we interpret the transition as a structural modification, whose magnitude is a function of the temperature and which results in a non-vanishing polarization at T_C . Starting from the transition temperature and moving towards lower temperatures, the polarization continuously grows. On top of this structural modification, the presence of structural defects and defect clusters will affect the atomic movement.

The structural modifications are detectable, to a certain extent, in transport and calorimetry experiments. Measurements

of the conductivity of both LT and LN demonstrate signatures of the structural modifications well below T_C , while the heat capacity is modified in a narrower interval, instead.

Finally, the Curie temperature of LN is found to be raised by Mg doping. Mg_{Li} substitutionals are found to locally pin the ferroelectric polarization, thus acting against thermal disorder. The presented AIMD calculations allow to investigate how dopants influence the Curie temperature of the samples and can be applied to other common dopants such as Ti, Fe, or Ni.

Another field in which a similar approach is expected to be of large benefit concerns the study of LNT solid solutions [78]. The solid solutions, grown specifically to combine the optical and acoustic properties of LN with the thermal stability of LT, represent a rather new field of research, for which the characterization of the thermal behavior will be of crucial relevance.

ACKNOWLEDGMENTS

We gratefully acknowledge financial support by the Deutsche Forschungsgemeinschaft (DFG) through the research group FOR5044 (Grant No. 426703838 [79], SA1948/3-1, SU1261/1-1, SCHM 1569/39-1, FR1301/42-1, GA 2403/7-1). Calculations for this research were conducted on the Lichtenberg high-performance computer of the TU Darmstadt and at the Höchstleistungsrechenzentrum Stuttgart (HLRS). The authors furthermore acknowledge the computational resources provided by the HPC Core Facility and the HRZ of the Justus-Liebig-Universität Gießen.

-
- [1] R. S. Weis and T. K. Gaylord, Lithium niobate: Summary of physical properties and crystal structure, *Appl. Phys. A* **37**, 191 (1985).
- [2] U. Yakhnevych, F. El Azzouzi, F. Bernhardt, C. Kofahl, Y. Suhak, S. Sanna, K.-D. Becker, H. Schmidt, S. Ganschow, and H. Fritze, Oxygen partial pressure and temperature dependent electrical conductivity of lithium- niobate-tantalate solid solutions, *Solid State Ionics* **407**, 116487 (2024).
- [3] T.-C. Lee, J.-T. Lee, M. A. Robert, S. Wang, and T. A. Rabson, Surface acoustic wave applications of lithium niobate thin films, *Appl. Phys. Lett.* **82**, 191 (2003).
- [4] S. Sanna and W. G. Schmidt, LiNbO₃ surfaces from a microscopic perspective, *J. Phys.: Condens. Matter* **29**, 413001 (2017).
- [5] A. Rüber, *Chemistry and Physics of Lithium nNiobate*, Current Topics in Materials Science (Elsevier Science Publishing, Amsterdam, 1978), Vol. 1.
- [6] T. Volk and M. Wöhlecke, *Lithium Niobate, Defects, Photorefraction and Ferroelectric Switching*, Springer Series in Materials Science (Springer, Berlin, 2009), Vol. 115.
- [7] Y.-L. Chen, J.-J. Xu, X.-J. Chen, Y.-F. Kong, and G.-Y. Zhang, Domain reversion process in near-stoichiometric LiNbO₃ crystals, *Opt. Commun.* **188**, 359 (2001).
- [8] K. Kitamura, Y. Furukawa, K. Niwa, V. Gopalan, and T. E. Mitchell, Crystal growth and low coercive field 180° domain switching characteristics of stoichiometric LiTaO₃, *Appl. Phys. Lett.* **73**, 3073 (1998).
- [9] M. Nakamura, S. Takekawa, S. Kumaragurubaran, and K. Kitamura, Curie temperature and [Li]/([Li] + [Nb]) ratio of near-stoichiometric LiNbO₃ crystal grown from different Li-rich solutions, *Jpn. J. Appl. Phys.* **47**, 3476 (2008).
- [10] Y. S. Kim and R. T. Smith, Thermal expansion of lithium tantalate and lithium niobate single crystals, *J. Appl. Phys.* **40**, 4637 (1969).
- [11] S. Sanna and W. G. Schmidt, Ferroelectric phase transition in LiNbO₃: Insights from molecular dynamics, *IEEE Trans. Ultrason. Ferroelectr. Freq. Control.* **59**, 1925 (2012).
- [12] S. R. Phillpot and V. Gopalan, Coupled displacive and order-disorder dynamics in LiNbO₃ by molecular-dynamics simulation, *Appl. Phys. Lett.* **84**, 1916 (2004).
- [13] S. Sanna, S. Neufeld, M. Rüsing, G. Berth, A. Zrenner, and W. G. Schmidt, Raman scattering efficiency in LiTaO₃ and LiNbO₃ crystals, *Phys. Rev. B* **91**, 224302 (2015).
- [14] S. Margueron, A. Bartaszyte, A. M. Glazer, E. Simon, J. Hlinka, I. Gregora, and J. Gleize, Resolved E-symmetry zone-centre phonons in LiTaO₃ and LiNbO₃, *J. Appl. Phys.* **111**, 104105 (2012).
- [15] M. Friedrich, A. Riefer, S. Sanna, W. G. Schmidt, and A. Schindlmayr, Phonon dispersion and zero-point

- renormalization of LiNbO_3 from density-functional perturbation theory, *J. Phys.: Condens. Matter* **27**, 385402 (2015).
- [16] A. Ridah, P. Bourson, M. D. Fontana, and G. Malovichko, The composition dependence of the Raman spectrum and new assignment of the phonons in LiNbO_3 , *J. Phys.: Condens. Matter* **9**, 9687 (1997).
- [17] M. Friedrich, A. Schindlmayr, W. G. Schmidt, and S. Sanna, LiTaO_3 phonon dispersion and ferroelectric transition calculated from first principles, *Physica status solidi (b)* **253**, 683 (2016).
- [18] V. Caciuc and A. V. Postnikov, *Ab initio* zone-center phonons in LiTaO_3 : Comparison to LiNbO_3 , *Phys. Rev. B* **64**, 224303 (2001).
- [19] C. Raptis, Assignment and temperature dependence of the Raman modes of LiTaO_3 studied over the ferroelectric and paraelectric phases, *Phys. Rev. B* **38**, 10007 (1988).
- [20] A. S. Barker and R. Loudon, Dielectric properties and optical phonons in LiNbO_3 , *Phys. Rev.* **158**, 433 (1967).
- [21] W. D. Johnston and I. P. Kaminow, Temperature dependence of Raman and Rayleigh scattering in LiNbO_3 and LiTaO_3 , *Phys. Rev.* **168**, 1045 (1968).
- [22] J. Servoin and F. Gervais, Soft vibrational mode in LiNbO_3 and LiTaO_3 , *Solid State Commun.* **31**, 387 (1979).
- [23] I. G. Wood, P. Daniels, R. H. Brown, and A. M. Glazer, Optical birefringence study of the ferroelectric phase transition in lithium niobate tantalate mixed crystals: $\text{LiNb}_{1-x}\text{Ta}_x\text{O}_3$, *J. Phys.: Condens. Matter* **20**, 235237 (2008).
- [24] M. R. Chowdhury, G. E. Peckham, R. T. Ross, and D. H. Saunderson, Lattice dynamics of lithium niobate, *J. Phys. C* **7**, L99 (1974).
- [25] S. Kojima, Order-disorder nature of ferroelectric phase transition in stoichiometric LiNbO_3 crystals, *Ferroelectrics* **223**, 63 (1999).
- [26] A. F. Penna, A. Chaves, P. d. R. Andrade, and S. P. S. Porto, Light scattering by lithium tantalate at room temperature, *Phys. Rev. B* **13**, 4907 (1976).
- [27] I. Inbar and R. E. Cohen, Comparison of the electronic structures and energetics of ferroelectric LiNbO_3 and LiTaO_3 , *Phys. Rev. B* **53**, 1193 (1996).
- [28] J. Yu and K.-T. Park, First principles total energy study of ferroelectric transitions in LiNbO_3 , *Phys. B: Condens. Matter* **237-238**, 341 (1997).
- [29] D. Lee, H. Xu, V. Dierolf, V. Gopalan, and S. R. Phillpot, Structure and energetics of ferroelectric domain walls in LiNbO_3 from atomic-level simulations, *Phys. Rev. B* **82**, 014104 (2010).
- [30] S. Sanna, C. Thierfelder, S. Wippermann, T. P. Sinha, and W. G. Schmidt, Barium titanate ground- and excited-state properties from first-principles calculations, *Phys. Rev. B* **83**, 054112 (2011).
- [31] Y. Fu, H. Wei, L. Wei, H. Zhang, X. Wang, B. Liu, Y. Zhang, X. Lv, J. Zhou, and H. Yu, Origin of the difference in thermal conductivity and anharmonic phonon scattering between LiNbO_3 and LiTaO_3 , *Cryst. Eng. Comm.* **23**, 8572 (2021).
- [32] B. Grabmaier and F. Otto, Growth and investigation of MgO-doped LiNbO_3 , *J. Cryst. Growth* **79**, 682 (1986).
- [33] A. Riefer, S. Sanna, and W. G. Schmidt, $\text{LiNb}_{1-x}\text{Ta}_x\text{O}_3$ electronic structure and optical response from first-principles calculations, *Ferroelectrics* **447**, 78 (2013).
- [34] G. Kresse and J. Hafner, *Ab initio* molecular dynamics for liquid metals, *Phys. Rev. B* **47**, 558 (1993).
- [35] G. Kresse and J. Furthmüller, Efficient iterative schemes for *ab initio* total-energy calculations using a plane-wave basis set, *Phys. Rev. B* **54**, 11169 (1996).
- [36] G. Kresse and J. Furthmüller, Efficiency of *ab-initio* total energy calculations for metals and semiconductors using a plane-wave basis set, *Comput. Mater. Sci.* **6**, 15 (1996).
- [37] P. E. Blöchl, Projector augmented-wave method, *Phys. Rev. B* **50**, 17953 (1994).
- [38] G. Kresse and D. Joubert, From ultrasoft pseudopotentials to the projector augmented-wave method, *Phys. Rev. B* **59**, 1758 (1999).
- [39] J. P. Perdew, A. Ruzsinszky, G. I. Csonka, O. A. Vydrov, G. E. Scuseria, L. A. Constantin, X. Zhou, and K. Burke, Restoring the density-gradient expansion for exchange in solids and surfaces, *Phys. Rev. Lett.* **100**, 136406 (2008).
- [40] S. L. Dudarev, G. A. Botton, S. Y. Savrasov, C. J. Humphreys, and A. P. Sutton, Electron-energy-loss spectra and the structural stability of nickel oxide: An LSDA+U study, *Phys. Rev. B* **57**, 1505 (1998).
- [41] A. Krampf, M. Imlau, Y. Suhak, H. Fritze, and S. Sanna, Evaluation of similarities and differences of LiTaO_3 and LiNbO_3 based on high-t-conductivity, nonlinear optical fs-spectroscopy and *ab initio* modeling of polaronic structures, *New J. Phys.* **23**, 033016 (2021).
- [42] J. D. Pack and H. J. Monkhorst, "Special points for Brillouin-zone integrations"-A reply, *Phys. Rev. B* **16**, 1748 (1977).
- [43] A. Togo, L. Chaput, I. Tanaka, and G. Hug, First-principles phonon calculations of thermal expansion in Ti_3SiC_2 , Ti_3AlC_2 , and Ti_3GeC_2 , *Phys. Rev. B* **81**, 174301 (2010).
- [44] A. Togo, First-principles phonon calculations with phonopy and phono3py, *J. Phys. Soc. Jpn.* **92**, 012001 (2023).
- [45] A. Togo and I. Tanaka, First principles phonon calculations in materials science, *Scr. Mater.* **108**, 1 (2015).
- [46] K. Parlinski, Z. Q. Li, and Y. Kawazoe, First-principles determination of the soft mode in cubic ZrO_2 , *Phys. Rev. Lett.* **78**, 4063 (1997).
- [47] See Supplemental Material at <http://link.aps.org/supplemental/10.1103/PhysRevMaterials.8.054406> for the corresponding data for LiNbO_3 , as well as a table with the unit cell volume and the lattice parameters calculated for each considered temperature.
- [48] L. Monacelli, R. Bianco, M. Cherubini, M. Calandra, I. Errea, and F. Mauri, The stochastic self-consistent harmonic approximation: Calculating vibrational properties of materials with full quantum and anharmonic effects, *J. Phys.: Condens. Matter* **33**, 363001 (2021).
- [49] I. Errea, M. Calandra, and F. Mauri, First-principles theory of anharmonicity and the inverse isotope effect in superconducting palladium-hydride compounds, *Phys. Rev. Lett.* **111**, 177002 (2013).
- [50] I. Errea, M. Calandra, and F. Mauri, Anharmonic free energies and phonon dispersions from the stochastic self-consistent harmonic approximation: Application to platinum and palladium hydrides, *Phys. Rev. B* **89**, 064302 (2014).
- [51] R. Bianco, I. Errea, L. Paulatto, M. Calandra, and F. Mauri, Second-order structural phase transitions, free energy curvature, and temperature-dependent anharmonic

- phonons in the self-consistent harmonic approximation: Theory and stochastic implementation, *Phys. Rev. B* **96**, 014111 (2017).
- [52] L. Monacelli, I. Errea, M. Calandra, and F. Mauri, Pressure and stress tensor of complex anharmonic crystals within the stochastic self-consistent harmonic approximation, *Phys. Rev. B* **98**, 024106 (2018).
- [53] See Supplemental Material at <http://link.aps.org/supplemental/10.1103/PhysRevMaterials.8.054406> for more data concerning the SSCHA procedure.
- [54] See Supplemental Material at <http://link.aps.org/supplemental/10.1103/PhysRevMaterials.8.054406> for the SSCHA calculated phonon dispersion of LiTaO₃ and LiNbO₃.
- [55] S. Nosé, A unified formulation of the constant temperature molecular dynamics methods, *J. Chem. Phys.* **81**, 511 (1984).
- [56] B. L. Holian, A. F. Voter, and R. Ravelo, Thermostatted molecular dynamics: How to avoid the Toda demon hidden in Nosé-Hoover dynamics, *Phys. Rev. E* **52**, 2338 (1995).
- [57] R. Resta, Macroscopic polarization in crystalline dielectrics: The geometric phase approach, *Rev. Mod. Phys.* **66**, 899 (1994).
- [58] R. D. King-Smith and D. Vanderbilt, Theory of polarization of crystalline solids, *Phys. Rev. B* **47**, 1651 (1993).
- [59] R. Resta, Macroscopic electric polarization as a geometric quantum phase, *Europhys. Lett.* **22**, 133 (1993).
- [60] See Supplemental Material at <http://link.aps.org/supplemental/10.1103/PhysRevMaterials.8.054406> for more details about the calculation of P_5 .
- [61] The figure shows a gaussian fit of the raw data. See Supplemental Material at <http://link.aps.org/supplemental/10.1103/PhysRevMaterials.8.054406> for the raw data.
- [62] Z.-G. Zhang, T. Abe, C. Moriyoshi, H. Tanaka, and Y. Kuroiwa, Synchrotron-radiation X-ray diffraction evidence of the emergence of ferroelectricity in LiTaO₃ by ordering of a disordered Li ion in the polar direction, *Appl. Phys. Express* **11**, 071501 (2018).
- [63] F. El Azzouzi, D. Klimm, L. M. Verhoff, N. A. Schäfer, S. Ganschow, K.-D. Becker, S. Sanna, and H. Fritze, Evolution of the electrical conductivity of LiNb_{1-x}Ta_xO₃ solid solutions across the ferroelectric phase transformation, *Phys. Stat. Solidi (a)*, doi: 10.1002/pssa.202300966.
- [64] U. Bashir, K. Böttcher, D. Klimm, S. Ganschow, F. Bernhardt, S. Sanna, M. Rüsing, L. M. Eng, and M. Bickermann, Solid solutions of lithium niobate and lithium tantalate: Crystal growth and the ferroelectric transition, *Ferroelectrics* **613**, 250 (2023).
- [65] Y. Zou, S. Xiang, and C. Dai, Investigation on the efficiency and accuracy of methods for calculating melting temperature by molecular dynamics simulation, *Comput. Mater. Sci.* **171**, 109156 (2020).
- [66] See Supplemental Material at <http://link.aps.org/supplemental/10.1103/PhysRevMaterials.8.054406> for a comparison of the values calculated with and without thermal expansion.
- [67] Y. Li, L. Li, X. Cheng, and X. Zhao, Microscopic properties of Mg in Li and Nb sites of LiNbO₃ by first-principle hybrid functional: Formation and related optical properties, *J. Phys. Chem. C* **121**, 8968 (2017).
- [68] F. Nitanda, Y. Furukawa, S. Makio, M. Sato, and K. I. K. Ito, Increased optical damage resistance and transparency in MgO-Doped LiTaO₃ single crystals, *Jpn. J. Appl. Phys.* **34**, 1546 (1995).
- [69] D. A. Bryan, R. Gerson, and H. E. Tomaschke, Increased optical damage resistance in lithium niobate, *Appl. Phys. Lett.* **44**, 847 (1984).
- [70] See Supplemental Material at <http://link.aps.org/supplemental/10.1103/PhysRevMaterials.8.054406> for the calculated band structure of Mg doped LiNbO₃.
- [71] Y. Furukawa, K. Kitamura, A. Alexandrovski, R. K. Route, M. M. Fejer, and G. Foulon, Green-induced infrared absorption in MgO doped LiNbO₃, *Appl. Phys. Lett.* **78**, 1970 (2001).
- [72] T. U. of Sheffield, WebElements, <https://www.webelements.com> (2023), last accessed 10th October 2023.
- [73] See Supplemental Material at <http://link.aps.org/supplemental/10.1103/PhysRevMaterials.8.054406> for a comparison of the experimental data from transport and calorimetry measurements with the theoretically predicted temperature dependent order parameter (e.g., the spontaneous polarization).
- [74] Y. Li, W. G. Schmidt, and S. Sanna, Defect complexes in congruent LiNbO₃ and their optical signatures, *Phys. Rev. B* **91**, 174106 (2015).
- [75] H. Xu, D. Lee, J. He, S. B. Sinnott, V. Gopalan, V. Dierolf, and S. R. Phillpot, Stability of intrinsic defects and defect clusters in LiNbO₃ from density functional theory calculations, *Phys. Rev. B* **78**, 174103 (2008).
- [76] A. Vyalikh, M. Zschornak, T. Köhler, M. Nentwich, T. Weigel, J. Hanzig, R. Zaripov, E. Vavilova, S. Gemming, E. Brendler, and D. C. Meyer, Analysis of the defect clusters in congruent lithium tantalate, *Phys. Rev. Mater.* **2**, 013804 (2018).
- [77] C. Kofahl, L. Dörrer, B. Muscutt, S. Sanna, S. Hurskyy, U. Yakhnevych, Y. Suhak, H. Fritze, S. Ganschow, and H. Schmidt, Li self-diffusion and ion conductivity in congruent LiNbO₃ and LiTaO₃ single crystals, *Phys. Rev. Mater.* **7**, 033403 (2023).
- [78] F. Bernhardt, F. A. Pfeiffer, F. Schug, S. Sanna, A. Pfannstiel, T. Hehemann, M. Imlau, and S. Ganschow, *Phys. Rev. Mater.* (to be published).
- [79] S. Ganschow, H. Schmidt, Y. Suhak, M. K. Imlau, M. Rüsing, L. M. Eng, H. Fritze, and S. Sanna, Periodic low-dimensional defect structures in polar oxides (2021), <https://www.for5044.de/en/>.